Three dimensional imaging of shear bands in bulk metallic glass composites

Allen H. Hunter [1], Vicente Araullo-Peters [1], Michael Gibbons[2], Oscar D. Restrepo[2], Stephen R. Niezgoda[2], Wolfgang Windl [2], Katharine M. Flores [3], Douglas C. Hofmann [4], Emmanuelle A. Marquis [1,*]

[1] Department of Materials Science and Engineering, University of Michigan, Ann Arbor, MI 48109

[2] Department of Materials Science and Engineering, The Ohio State University, Columbus, OH 43210

[3] Department of Mechanical Engineering and Materials Science, Institute of Materials Science and Engineering, Washington University, St. Louis, MO 63130

[4] Jet Propulsion Laboratory/California Institute of Technology, Pasadena, CA 91109

***Corresponding author**

Phone: (734) 764 8717

Email: emarq@umich.edu

Address: 2300 Hayward St, Ann Arbor MI 48109

Abstract

The mechanism of the increase in ductility in bulk metallic glass matrix composites (BMGMCs) over monolithic bulk metallic glasses (BMGs) is to date little understood, primarily because the interplay between dislocations in the crystalline phase and shear bands in the glass could neither be imaged nor modeled in a validated way. To overcome this roadblock, we show that shear bands can be imaged in three dimensions by atom probe tomography from density variations in the reconstructed atomic density, which density-functional theory suggests being a local-work function effect. Imaging of near-interface shear

This is the author manuscript accepted for publication and has undergone full peer review but has not been through the copyediting, typesetting, pagination and proofreading process, which may lead to differences between this version and the Version of Record. Please cite this article as doi: 10.1111/jmi.12443.

bands in $Ti_{48}Zr_{20}V_{12}Cu_5Be_{15}$ BMGMC permits measurement of their composition, thickness, branching, and interactions with the dendrite interface. These results confirm that shear bands here nucleate from stress concentrations in the glass due to intense, localized plastic deformation in the dendrites rather than intrinsic structural inhomogeneities.

Keywords

shear band; atom probe tomography; density-functional theory

Bulk metallic glass matrix composites combine the structure and properties of two different phases: a metallic glass phase and a crystalline phase, making them both strong and ductile. How can we better design these materials so they deform without breaking is the key question of this paper, which we address by imaging locally the regions where the material has deformed. Because of the complex arrangement of the two phases, we use an imaging technique (atom probe tomography) that provides 3D spatial information and we are able to reveal local deformation at the atomic scale, which we support and confirm using modeling.

Introduction

Bulk metallic glass materials combine a very high yield strength with the ability to be intricately formed into net shape components using relatively low temperature forging above the material's glass transition temperature. However, at temperatures below the glass transition, BMGs frequently display very limited ductility and catastrophic failure due to the

propagation of shear bands, which are zones with strongly localized deformation. To improve ductility, BMGMCs have been proposed where a crystalline dendritic network can redistribute load through dislocation slip (Hays 2000). While on the macroscopic level, there is agreement that the crystalline phase blocks the long-range propagation of shear bands and thus preempts catastrophic failure in BMGMCs, their formation, propagation, and interactions with the reinforcing crystalline phase remain under discussion (Chen 2012; Chen 2013; Jeon 2013; Zhang 2014), making targeted improvement of BMGMC alloys very difficult.

Arguably, the largest uncertainties exist concerning the formation processes of shear bands in BMGMCs. While shear bands are often found to originate from structural flaws such as voids or surface features, which act as stress concentrations, their formation in monolithic glasses is typically discussed in terms of local inhomogeneities on the level of the ambiguously defined shear transformation zones (STZ) (Argon 1979). For BMGMCs, no fundamentally different nucleation mechanism is assumed, and the interplay between deformation mechanisms in the crystalline dendrites and shear band formation in the glass matrix that can lead to large ductility, such as observed for $Ti_{48}Zr_{20}V_{12}Cu_5Be_{15}$ BMGMC, is little understood.

Also, shear bands usually appear as a change in the local free volume, which is defined as the volume in excess of an ideal amorphous structure. At times, the structural changes in shear bands are so severe that crystalline phases (Jiang 2006) or nanovoids (Li 2002) have been observed following deformation. While changes in local free volume in shear bands is little disputed in the current literature, large discrepancies exist about their magnitude. Traditionally, localization of strain in shear bands has been associated with increased free volume, or equivalently lower density. This increase ranges from small changes of 1-2% measured with nanobeam diffraction (Chen 2009) to changes as large as 11% suggested by

transmission electron microscopy imaging (Donovan 1981). To add even larger spread, recent high angle annular dark field (HAADF) scanning transmission electron microscopy (STEM) work reported a decrease in free volume within shear bands (Shao 2013) with a range of density changes from −10% to + 6.3% (Rösner 2014). The variations are currently unexplained, with possible reasons ranging from stick-slip like shearing in shear bands to artifacts related to the 2D projection in Z-contrast imaging.

In order to clarify the nature of shear bands, we apply a three-dimensional imaging method based on atom probe tomography (APT), which in combination with STEM imaging and modeling on both atomic and continuum scales gives new key insights into the deformation mechanisms and interplay between the crystalline and glass phases in BMGMCs.

Experimental methods and results

A $Ti_{48}Zr_{20}V_{12}Cu_5Be_{15}$ glass composite was arc melted under vacuum and rapidly chilled in a water-cooled copper mold. The sample was machined into a tension test sample and pulled in tension until failure, resulting in a highly deformed necked region with a high density of shear bands.

Samples for atom probe tomography and transmission electron microscopy were prepared using a FEI Helios Nanolab 650 DualBeam FIB (FEI, Eindhoven, The Netherlands). TEM samples were analyzed using a JEOL (Peabody, MA, USA) 2100F TEM/STEM equipped with a spherical aberration corrector at 200 kV accelerating voltage. Images were recorded in STEM mode with high angle annular dark field (HAADF) detectors and were analyzed using ImageJ (Schneider 2012). APT samples were analyzed using a Cameca (Madison, WI, USA) LEAP 4000X HR atom probe instrument operated in laser pulsed mode. The samples were field evaporated at 25 K using 10 pJ laser pulse energy and 250 kHz pulse repetition rate,

with a nominal detection rate of 0.5%. Reconstruction and visualization were performed using the Cameca software IVAS 3.6. Sample geometry was measured before and after APT, and was used to calculate the evaporation field and image compression factor (ICF) needed for the data reconstruction algorithm. Typical values were 42 V/nm for the field strength and ICFs ranging from 1.4 to 1.7. Local densities are calculated from counting the number of ions within a sphere of fixed radius centered on each individual ion. The choice of the radius requires a tradeoff between statistical uncertainty in the local density from too small a radius and loss of spatial resolution from a radius that is too large. A value of 1.0 nm was used for this analysis. The shear bands were then imaged using the reconstructed atomic density.

Our APT method is based on density variations, which were first analyzed with HAADF STEM imaging in order to define the density range present. In **Figure 1**, the shear bands, which were aligned parallel to the electron beam, are clearly discernible in the amorphous matrix, appearing darker than the surrounding matrix. This is consistent with a slight reduction in density (or increase in free volume) in the shear bands compared to the surrounding matrix (Rösner 2014). Measurements of relative intensity changes across the shear bands suggest an average density change of −3% ± 1% using the full width at half maximum (FWHM) of the density plot to determine the limits, over a gradient of ~3 nm, while no decrease in free volume was found.

The deformed structures analyzed by APT reveal shear band regions with higher reconstructed atomic density, in contrast to the HAADF results, which makes them visible in **Figure 2**. The shear bands are observed in the glass matrix and also near and intersecting the dendrite interface. The thickness of the individual shear bands ranges from 3.4 to 10 nm, with an average thickness (or FWHM of the density peak) of 6 ± 1.5 nm. This can be

compared to known characteristic shear band thickness of ~10 nm (Zhang 2006). No detectable chemistry change was measured through 1D concentration analysis perpendicular to the band (**Figure 2(b)**), which is consistent with previous APT studies (Chen 2009; Guo 2014). In addition, no evidence of local chemical clustering was detected. Quantitatively, the shear band regions exhibit an average reconstructed atomic density increase of 20 % ranging from 7% to 60 % (**Figure 2(c)).**

Modeling

To understand the apparent contradiction between the shear band densities observed by APT and HAADF, we examined the dependence of the evaporation field on the density of the sample using density-functional theory (DFT) calculations using within the image-hump model (Müller 1956). Although the underlying model has been criticized (Miller 2014) and does not produce correct escape distances (Yao 2015), previous DFT work has suggested that it agrees with field-dependent calculations for Al in the evaporation regime rather well (Sanchez 2004). Within the image-hump model (Müller 1956), the evaporation field in the low-temperature limit is given by

$$F_0^{n+} = 4\rho(ne)^{-3}\left(Q_{n+}^0\right)^2, \qquad (1)$$

where *ne* is the escape charge and Q_{n+}^0 is a thermodynamic term given by $Q_{n+}^0 = H_b + I_{n+} - nf$, which can be calculated from the binding enthalpy of the (neutral) atom H_b , its ionization energy from charge 0 to $n+$, I_{n+}, and the local work function ϕ (Smith 1930). The neutral-atom binding energy was calculated as the enthalpy ($H = E_{\text{tot}} + pV$) difference between the perfect surface with an isolated atom in the center of the vacuum layer and the perfect surface with an adatom on the hollow site. We used the DFT code VASP (Kresse 1994) with PAW potentials within PW-91 spin-resolved GGA (Perdew 1992) with 240 eV cutoff energy. Work

function and neutral-atom binding energy are calculated with 3x3x3 supercells of the conventional fcc unit cell with 108 atoms, a 1.5 nm vacuum and relaxed (100) surfaces with 4x4x1 k-point Brillouin zone sampling. The entire structure was scaled isotropically to examine different densities that were calculated from the in-plane lattice constants. The work function was calculated from the difference between the calculated electrostatic potential in the center of the vacuum and the calculated Fermi energy and is 4.23 eV for the relaxed cell, very close to the experimental value of 4.24 eV. The ionization energy is calculated from the energy difference between neutral and charged atoms in vacuum for different simulation cell sizes a between 15 and 3.0 nm side length and extrapolated to infinity by fitting $E(a) = E_\infty - E'/a$. It is found to be 6.04 eV for Al^+ and 24.87 eV for Al^{++}, in good agreement with experimental values of 5.99 and 24.81 eV (Lide 2003). For the relaxed structure, we find binding energies Q_1^0 = 4.9 eV and Q_2^0 = 19.4 eV, resulting in zero-temperature evaporation fields F_o^1 = 17 V/nm and F_o^2 = 33 V/nm, in good agreement with previously calculated values of 19 and 35 V/nm, respectively (Tsong 1978).

Significantly decreasing computational uncertainties and cost by substituting a BMG structure with an isolated adatom on an Al surface, allows us then to derive a scaling law for the change in evaporation field with density. The simulation cell was scaled isotropically and its density was calculated from the in-plane lattice constants. **Figure 3** shows the results for relative changes in heat of evaporation (sum of total energy of evaporation plus pV term for the bulk of the slab), work function, and resulting activation energy as a function of atom density relative to the minimum-energy density at 62.03 atoms/nm^3. Note that the ionization energy of the ion is independent of the bulk density. While the binding enthalpy is approximately symmetric around the minimum volume with little skew from the pV term, the work function is monotonically increasing with decreasing density. This results in the overall

binding energy and thus evaporation field decreasing as a function of decreasing density, in agreement with our experimental finding. Thus, we find that it is the density dependence of the local work function that ultimately causes the artifact of higher observed densities in APT for lower-density material. This modeling prediction can be further validated by looking at the charge state ratios of the evaporating ions.

In order to determine the dependence of the charge-state ratio on density for an ion species with charges *n* and *m*, we start from the density-dependent activation energy for field evaporation for the two charge states in the presence of the field, which is given by (Müller 1956):

$$Q_{n+}(F,r) = H_b(r) + I_{n+} - nf(r) - \sqrt{\frac{n^3 e^3 F}{4\pi\varepsilon_0}}. \qquad (2)$$

Due to the limitations of image hump model, we examine here if it is sufficient for our purposes and describes the barrier dependence on field reasonably well in the range where the barrier disappears, i.e., where field evaporation happens. For that, we plot in **Figure 4** the results from (Sanchez 2004), along with barrier vs. field derived from the image hump model (**Eq. 2**) using the barrier value of 3.6 eV for F = 0, i.e. $Q_{1+}(F) = Q_{1+}^{\text{Sanchez}}(F=0) - \sqrt{\frac{n^3 e^3 F}{4\pi\varepsilon_0}}$. Evaporation happens where the barrier disappears, i.e. for fields around 19 V/nm. As can be seen, the value for the evaporation field, as well as the slope of barrier vs. field, show rather good agreement between image-hump prediction and directly calculated values. Thus, independently of if this agreement is physical or fortuitous, it means that **Eq. (2)** along with **Eq. (1)** in the main text provide a model to derive the dependence of zero-barrier evaporation fields on density.

Since the evaporation rates r_{n+} can be assumed to follow an Arrhenius behavior,

$$r_{n+}(F,r) = r_0 \exp\left(-\frac{Q_{n+}(F,r)}{kT}\right), \quad (3)$$

the change in evaporation rate ratio with density is given by

$$\frac{r_{n+}(F,r)}{r_{m+}(F,r)} = \exp\left(-\frac{Q_{n+}(F,r) - Q_{m+}(F,r)}{kT}\right), \quad (4)$$

assuming that the dependence of the prefactor on density can be neglected, which has been shown previously to be a good approximation for bulk-activated processes (Laudon 2001). Since the density-dependence of the work function dominates that of the binding enthalpy (**Figure 4**), the overall relative change in charge-state ratio for two densities ρ_1 and ρ_2 is then given by the density-dependence of the work function,

$$R_{n+/m+}(r_1, r_2) = \left[\frac{r_{n+}(F,r_1)}{r_{m+}(F,r_1)}\right] \Big/ \left[\frac{r_{n+}(F,r_2)}{r_{m+}(F,r_2)}\right] = \exp\left[(n-m)\frac{f(r_1) - f(r_2)}{kT}\right]. \quad (5)$$

If we assume that the increase in work function of +6.8 meV for 3% density decrease calculated for Al is typical and that the evaporation temperature is in the range of 25 to 90 K, we would expect an increase in the charge state ratio of ~0.04 to 0.4. The experimentally measured Zr^{2+}/Zr^{3} ratio is enhanced by ~20% within the shear band compared to the matrix (**Figure 2(d)**), which is of similar order of magnitude. The lowered evaporation field leads to increased evaporation rate locally, which manifests itself as a dip in the specimen surface and thus locally focused ion trajectories with adjacent matrix atoms projected into the same region of the detector as the shear band atoms. However, if properly exploited, the presence of such an artifact is not detrimental to APT analysis, but rather a powerful imaging tool as demonstrated by the present study.

Material microstructure and properties

Without exception, all visible shear bands either terminate at the matrix/dendrite interface or at other shear bands. No evidence could be found of shear bands originating or terminating within the glass matrix. This suggests that processes occurring at the glass/crystalline interface initiate shear bands in the glass, rather than structural inhomogeneities within the glass itself. Furthermore, the observations suggest that localized slip activity within the crystalline phase and associated interfacial steps are coupled with shear band nucleation, propagation and linking of the slip planes from one dendrite arm to another. A range of step heights linking dislocation channels in the dendrites with shear bands in the glass was observed. Where significant deformation had taken place, the shear bands are all connected with 20-50 nm (~50-150 Burgers vector lengths) or higher steps at the matrix/dendrite interface (**Figure 1(a)**). In **Figure 1(b)**, the interfacial steps are significantly smaller (< 10 nm), which agrees well with the APT reconstructions in **Figure 5**. In both dendrites in **Figure 1(b)**, dislocation channels are also visible where the shear bands initiated or terminated. While slip in the crystalline phase is not visible in the APT data in **Figure 5**, close examination of the Be distribution shows Be segregation in a plane parallel to the shear direction in the dendrite, presumably decorating a dislocation channel.

The APT data show a denser and more complex distribution of shear bands that would not be visible from the TEM thin foils due to tilting requirements. In fact, the shear steps shown in **Figure 5** are not parallel to each other but rather offset, which may be indicative of the slip system involved in deformation of the crystalline dendrite phase.

The observed deformed structures make the suggestion that in the BMGMCs studied, shear band formation is triggered by strong stress localization at the dendrite/glass interface, rather than from STZ-type matrix inhomogeneities. It is not the step at the interface that nucleates the shear band, but instead the formation of the shear band that produces the step through a

coordinated process over a short time period, as further demonstrated elsewhere using detailed micromechanical modeling (Gibbons, 2016). Once a sufficient amount of free volume has accumulated along some path through the matrix, and the stress along this path is relatively high due to the irregular microstructure and accumulation of strain at the interface, the conditions are ripe for rapid shear localization in the form of a shear band. The shear band rapidly propagates across the amorphous matrix terminating at another dendrite. Further propagation of the shear band across multiple dendrites is blocked by the activation of multiple slip systems in the dendritic regions; blunting the intense shear localization. Furthermore, structural inhomogeneities and shear transformation zones in the glass, which in the absence of such externally (dendrite) driven stress localization control shear band formation, seem to play less of a role for strain localization in the amorphous phase of BMGMCs. Following, the ductility of BMGMCs may be further improved by incorporating or engineering dendritic phases that can better dissipate large shear localizations through mechanisms such as micro-twinning or stress-driven martensitic transformations, as previously observed in select BMGC systems (Oh 2011).

Conclusions

We illustrate a 3D characterization method for shear bands in metallic glasses based on atom probe tomography. By accompanying STEM imaging and DFT calculations the apparent enhanced density, a technique artifact, is explained by an increase in the local work function that lowers the local evaporation field. This method allows full characterization of the shear band structures, which we have examined for a $Ti_{48}Zr_{20}V_{12}Cu_5Be_{15}$ BMGMC.

Acknowledgements

The authors wish to acknowledge financial support from the Air Force Office of Scientific Research Award No. FA9550-12-1-0059 with partial support from Award No. FA9550-14-1-0249 and from the University of Michigan College of Engineering, and computational support by the Ohio Supercomputer Center under Grant No. PAS0072. Part of this research was carried out at the Jet Propulsion Laboratory, California Institute of Technology, under a contract with the National Aeronautics and Space Administration (NASA).

References

Argon, A. S. (1979). "Plastic deformation in metallic glasses." Acta Metallurgica **27**(1): 47-58.

Chen, G., J. L. Cheng and C. T. Liu (2012). "Large-sized Zr-based bulk-metallic-glass composite with enhanced tensile properties." Intermetallics **28**: 25-33.

Chen, J. H., M. Q. Jiang, Y. Chen and L. H. Dai (2013). "Strain rate dependent shear banding behavior of a Zr-based bulk metallic glass composite." Materials Science and Engineering: A **576**(0): 134-139.

Chen, Y., T. Okhubo, T. Mukai and K. Hono (2009). "Structure of shear bands in Pd40Ni40P20 bulk metallic glass." Journal of Materials Research **24**(1): 1.

Donovan, P. E. and W. M. Stobbs (1981). "The structure of shear bands in metallic glasses." Acta Metallurgica **29**(8): 1419-1436.

Gibbons, M., K. M. Flores, E.A. Marquis, W. Windl, S.R. Niezgoda (2016). " Shear Banding in Bulk Metallic Glass Matrix Composites with Dendrite Reinforcements." International Journal of Plasticity. In Review.

Guo, W., E. A. Jägle, P.-P. Choi, J. Yao, A. Kostka, J. M. Schneider and D. Raabe (2014). "Shear-Induced Mixing Governs Codeformation of Crystalline-Amorphous Nanolaminates." Physical Review Letters **113**(3): 035501.

Hays, C. C., C. P. Kim and W. L. Johnson (2000). "Microstructure Controlled Shear Band Pattern Formation and Enhanced Plasticity of Bulk Metallic Glasses Containing in situ Formed Ductile Phase Dendrite Dispersions." Physical Review Letters **84**(13): 2901-2904.

Jeon, C., C. Paul Kim, H. Seop Kim and S. Lee (2013). "Dendrite size and tensile ductility in Ti-based amorphous alloys containing ductile dendrites." Materials Science and Engineering: A **587**(0): 143-149.

Jiang, W. H. and M. Atzmon (2006). "Mechanically-assisted nanocrystallization and defects in amorphous alloys: A high-resolution transmission electron microscopy study." Scripta Materialia **54**: 333–336.

Kresse, G. and J. Hafner (1994). "Ab initio molecular-dynamics simulation of the liquid-metal amorphous-semiconductor transition in germanium." Physical Review B **49**(20): 14251-14269.

Laudon, M., N. N. Carlson, M. P. Masquelier, M. S. Daw and W. Windl (2001). "Multiscale modeling of stress-mediated diffusion in silicon: Ab initio to continuum." Applied Physics Letters **78**: 201.

Li, J., Z. L. Wang and T. C. Hufnagel (2002). "Characterization of nanometer-scale defects in metallic glasses by quantitative high resolution transmission electron microscopy." Physical Review B **65**: 144201.

Lide, D. R. (2003). CRC Handbook of Chemistry and Physics, 84th Edition. Section 10, Atomic, Molecular, and Optical Physics; Ionization Potentials of Atoms and Atomic Ions. Boca Raton, Florida, CRC Press.

Miller, M. K. and R. G. Forbes (2014). Atom Probe Tomography: The Local Electrode Atom Probe. New York, Springer.

Müller, E. (1956). "Field Desorption." Physical Review **102**(3): 618-624.

Oh, Y. S., C. P. Kim, S. Lee and N. J. Kim (2011). "Microstructure and tensile properties of high-strength high-ductility Ti-based amorphous matrix composites containing ductile dendrites." Acta Materialia **59**(19): 7277-7286.

Perdew, J. P., J. A. Chevary, S. H. Vosko, K. A. Jackson, M. R. Pederson, D. J. Singh and C. Fiolhais (1992). "Atoms, molecules, solids, and surfaces: Applications of the generalized gradient approximation for exchange and correlation." Physical Review B **46**(11): 6671-6687.

Rösner, H., M. Peterlechner, C. Kübel, V. Schmidt and G. Wilde (2014). "Density changes in shear bands of a metallic glass determined by correlative analytical transmission electron microscopy." Ultramicroscopy **142**: 1-9.

Sanchez, C. G., A. Y. Lozovoi and A. Alavi (2004). "Field-evaporation from first-principles." Molecular Physics **102**(9-10): 1045-1055.

Schneider, C. A., W. S. Rasband and K. W. Eliceiri (2012). "NIH Image to ImageJ: 25 years of image analysis." Nat Meth **9**(7): 671-675.

Shao, Y., K. Yao, M. Li and X. Liu (2013). "Two-zone heterogeneous structure within shear bands of a bulk metallic glass." Applied Physics Letters **103**: 171901.

Smith, L. (1930). "The Emission of Positive Ions from Tungsten and Molybdenum." Physical Review **35**(4): 381-395.

Tsong, T. T. (1978). "Field-Ion Image-Formation." Surface Science **70**(1): 211-233.

Yao, L., T. Withrow, O. D. Restrepo, W. Windl and E. A. Marquis (2015). Effects of the local structure dependence of evaporation fields on field evaporation behavior. Applied Physics Letters **107**, 241602

Zhang, T., H. Y. Ye, J. Y. Shi, H. J. Yang and J. W. Qiao (2014). "Dendrite size dependence of tensile plasticity of in situ Ti-based metallic glass matrix composites." Journal of Alloys and Compounds **583**(0): 593-597.

Zhang, Y. and A. L. Greer (2006). "Thickness of shear bands in metallic glasses." Applied Physics Letters **89**: 071907.

Figure captions

Figure 1: HAADF STEM images of shear bands in metallic glass matrix and corresponding shear steps on dendrite interfaces. The shear bands are observed to bend, branch, and intersect with other shear bands as they propagate from one dendrite arm to an adjacent arm. In b) the shear beans are decorated with red dots to depict the branching. The shear bands begin and terminate at shear steps on the dendrite interface.

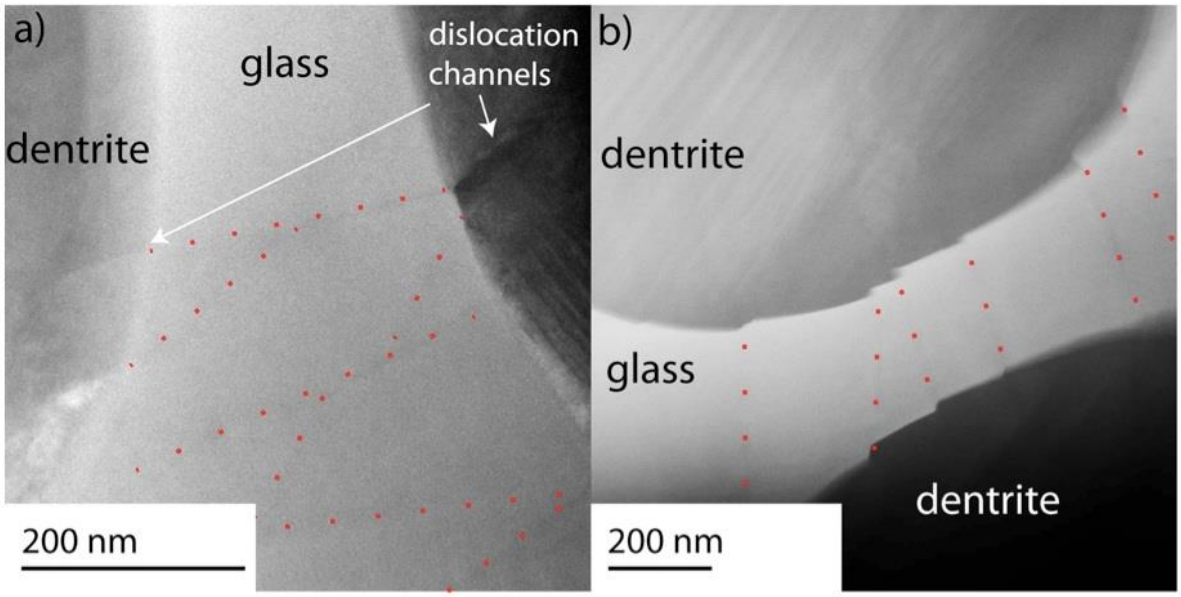

Figure 2: (a) APT reconstructions containing multiple shear bands. The interface between both phases is marked by a 34 at% Ti iso-concentration surface (red). 15% of the atoms with a local density greater than 90 at/nm^3 are shown by blue. (b) 1D Profile taken across representative shear band detected by APT. No significant concentration variation is detected between the SB and the matrix (b), but an increase in both reconstructed density (b) and Zr 2+/3+ charge state ratio (d) are observed within the shear band.

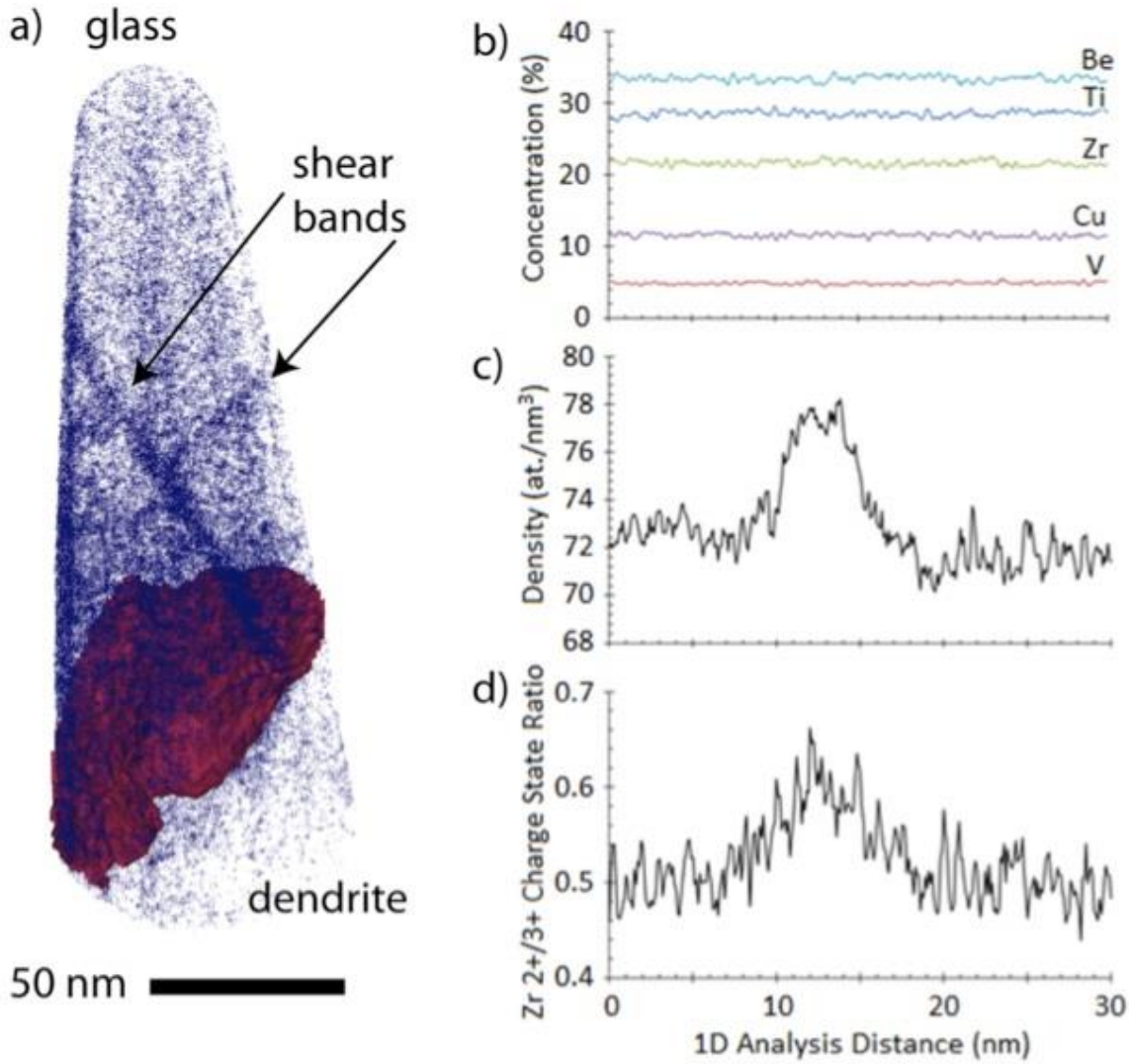

Figure 3: Dependence of the ion binding energy for Al+ and its components on the density in bulk Al as calculated by DFT. This shows that the evaporation field which is proportional to the square of the binding energy will decrease with decreasing density.

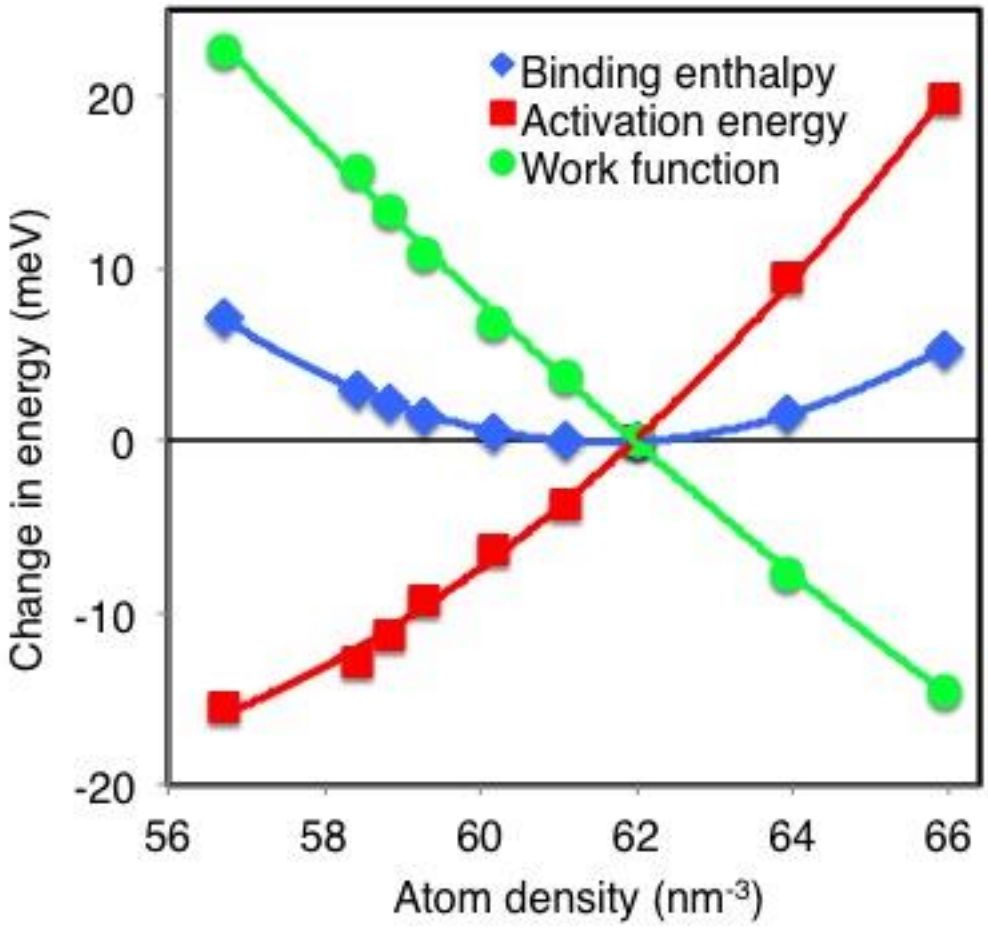

Figure 4: Barrier height vs. field, values from Ref. (Sanchez 2004) + image hump model for which the thermodynamic term is taken from Sanchez' value for zero field.

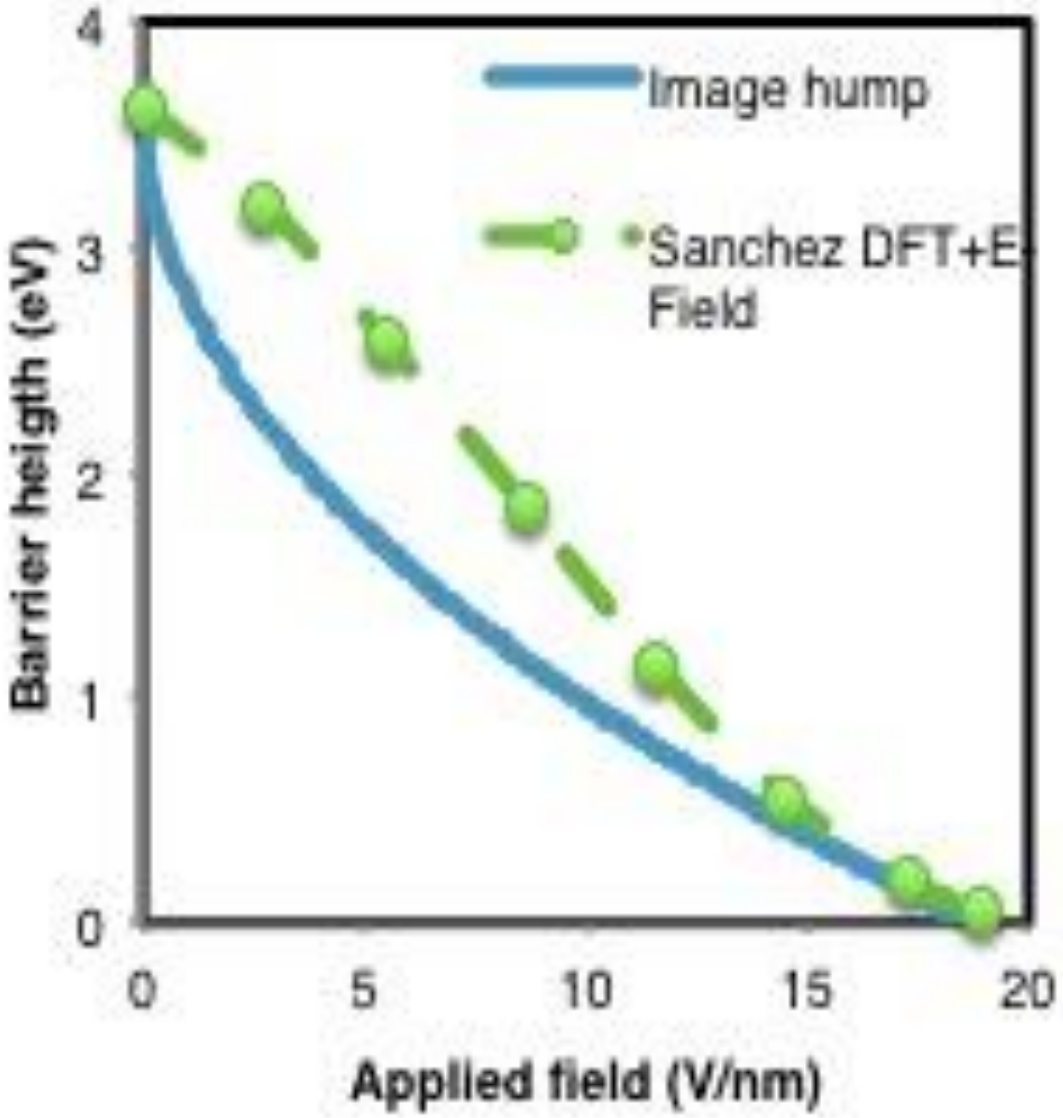

Figure 5: APT reconstruction showing shear bands terminating at the dendrite interface. (a) and (b) are rotated views of the same tip showing two shear steps at the interface. (c) is a top-down view of the 42% Ti isoconcentration surface showing both interface steps. (d) shows the partitioning map of Be across the dendrite-glass interface, which appears to segregate to the shear band near the step in the dendrite (c).